Particle-In-Cell Simulations of a Nonlinear Transverse Electromagnetic Wave in a Pulsar Wind Termination Shock

O. Skjæraasen

Institute of Theoretical Astrophysics, University of Oslo, PO Box 1029 Blindern, N-0315 Oslo, Norway.

olafsk@astro.uio.no

A. Melatos

School of Physics, University of Melbourne, Parkville, VIC 3010, Australia.

a.melatos@physics.unimelb.edu.au

A. Spitkovsky

KIPAC, Stanford University, PO Box 20450, MS 29, Stanford, CA 94309.

Chandra Fellow.

anatoly@slac.stanford.edu

ABSTRACT

A 2.5-dimensional particle-in-cell code is used to investigate the propagation of a large-amplitude, superluminal, nearly transverse electromagnetic (TEM) wave in a relativistically streaming electron-positron plasma with and without a shock. In the freestreaming, unshocked case, the analytic TEM dispersion relation is verified, and the streaming is shown to stabilize the wave against parametric instabilities. In the confined, shocked case, the wave induces strong, coherent particle oscillations, heats the plasma, and modifies the shock density profile via ponderomotive effects. The wave decays over $\gtrsim 10^2$ skin depths; the decay length scale depends primarily on the ratio between the wave frequency and the effective plasma frequency, and on the wave amplitude. The results are applied to the termination shock of the Crab pulsar wind, where the decay length-scale ($\gtrsim 0.05''$) might be comparable to the thickness of filamentary, variable substructure observed in the optical and X-ray wisps and knots.

Subject headings: pulsars: general — pulsars: individual (Crab Pulsar) — stars: neutron — shock waves — plasmas — outflows

1. INTRODUCTION

A rotation-powered pulsar emits most of its spin-down luminosity as a wind of relativistic particles, mainly electrons (e^-) and positrons (e^+) produced in pair cascades in charge-starved regions of the magnetosphere (Arons 2002). Observations of pulsar winds confined by supernova remnants (Hester et al. 2002) or the interstellar medium (Chatterjee & Cordes 2004; Gaensler et al. 2004) reveal that the wind terminates in a synchrotron-emitting shock with a cylindrically symmetric ('crossbow') morphology, implying that the outflow is collimated geometrically along the rotation axis, while the energy flux is concentrated in the equatorial plane (Komissarov & Lyubarsky 2004). The wind is launched from the light cylinder with most of its luminosity transported as Poynting flux (Coroniti 1990), and its enthalpy flux is negligible beyond the light cylinder r_L due to adiabatic cooling. On the other hand, models of the shock kinematics, the postshock flow, the synchrotron spectrum (Kennel & Coroniti 1984b), and the variability of shock substructure (e.g. wisps and knots in the Crab) (Spitkovsky & Arons 2004), strongly suggest that the ratio σ of Poynting flux to kinetic-energy flux is small at the shock, with $\sigma \sim 10^{-3}$ in several objects (Kennel & Coroniti 1984a; Gaensler et al. 2002).

In recent years, theoretical attention has focused on the radial structure of the wind, in order to explain how σ decreases from the magnetosphere ($\sigma \gg 1$) to the shock ($\sigma \ll 1$): the σ-paradox. The dissipation of Poynting flux seems to be related to the decay of the large-amplitude wave launched into the wind at the pulsar spin frequency. One possible cause is that ideal magnetohydrodynamics (MHD) breaks down beyond a critical radius r_c, in the sense that there are insufficient charge carriers to screen out the rest-frame electric field, and the electron inertia term in the relativistic Ohm's law becomes dominant (Melatos & Melrose 1996; Melatos 1998; Gedalin et al. 2001; Kuijpers 2001; Melatos 2002). In this respect, particular attention has been paid to the entropy wave carrying the alternating ('striped') magnetic field in the wind (Bogovalov 1999; Coroniti 1990) and its dissipation by magnetic reconnection at the corrugated current sheet separating the magnetic stripes (Lyubarsky & Kirk 2001), possibly emitting observable high-energy pulses (Arons 1979; Kirk et al. 2002; Kirk 2004; Skjæraasen 2004; Pétri & Kirk 2005). The dissipation occurs upstream from the termination shock, if the reconnection rate and particle flux are large enough (Kirk & Skjæraasen 2003), or else in the shock itself (Lyubarsky 2003).

In this Letter, we assess an alternative scenario in which, beyond r_c, the plasma upstream from the termination shock carries a superluminal *transverse electromagnetic (TEM)* wave, which modulates the wind and the shock (Melatos 2002). The wave is taken to be monochromatic, with a frequency given by the pulsar spin rate; an assumption generally used also in MHD wind models. Coherent particle acceleration in the TEM wave typically

leads to $\sigma \ll 1$; a self-consistent, WKB wave model predicts $\sigma \simeq 10^{-3}$ at the termination shock given the measured particle and energy fluxes of the Crab pulsar (Melatos & Melrose 1996; Melatos 1998). We use the 2.5-dimensional, relativistic, electromagnetic particle-in-cell (PIC) code XOOPIC (Verboncoeur et al. 1995) to investigate the free propagation of the wave upstream from the shock (§2), plasma heating in the shock (§3), and the fate of the wave inside and downstream from the shock (§3). We apply our results to the Crab pulsar wind in §4.

2. FREELY PROPAGATING TEM WAVES

A nonlinear TEM wave can propagate even if its frequency ω is less than the effective plasma frequency $\sqrt{2n^{\pm}e^2/\epsilon_0 m\gamma^{\pm}}$, where $n^{\pm}$ is the $e^{\pm}$ number density in the laboratory frame, m is the electron mass, and $\gamma^{\pm}$ is the Lorentz factor, because the wave forces charges to oscillate relativistically, increasing their effective mass. In a cold plasma, the plane wave dispersion relation is (Akhiezer & Polovin 1956; Kaw & Dawson 1970; Kennel & Pellat 1976; Melatos & Melrose 1996)

$$\eta^2 \;\; = \;\; 1 - \frac{2\omega_p^2}{\omega^2 \left(1 + E^2\right)^{1/2}}, \tag{1}$$

where $\eta = ck/\omega$ is the index of refraction, $\omega_p = \sqrt{n^{\pm}e^2/\epsilon_0 m\gamma_d}$, γ_d is the bulk Lorentz factor, and E is a dimensionless amplitude defined by $E = eE_0/mc\omega$, where E_0 is the physical electric field amplitude. For $E > 1$, the charges are accelerated from nonrelativistic to relativistic speeds within a single wave period. Note that a nonlinear electromagnetic wave is strictly transverse only if it is circularly polarised. In this case, the streaming speed $c\beta_d$ is a constant of the motion and can be chosen arbitrarily. As a result, $\sigma \propto E^2 \gamma_d^{-1}$ varies independently with E and γ_d, whereas in a linearly polarised nonlinear wave, γ_d (and hence σ) is determined uniquely by E. In the small-amplitude limit, $n^{\pm}, \gamma_d$ and E decouple.

In order to verify (1) with XOOPIC, we launch a cold $e^{\pm}$ beam from the left-hand edge ($x = 0$) of the simulation box. Two orthogonal, phased dipole antennas are placed at $x = 0$, continuously emitting a circularly polarised TEM wave with frequency $\omega = \omega_0$ which ramps up to a constant amplitude E over a rise time $t_{\rm r} \lesssim 0.2 t_{\rm c}$, where $t_{\rm c}$ is the time for the beam to cross the box. The right-hand edge of the box is transparent both to particles and waves (thanks to a wave-absorbing algorithm). Once initial transients disappear, we Fourier transform the transverse electric field component $E_z(x, t)$ and measure η for the Fourier component of largest amplitude. For linear waves with $10^{-4} < E < 10^{-1}$, we verify the linearized version of (1) to approximately 0.5 per cent in vacuo, 1 per cent in a uniform,

cold stationary plasma, and 2 per cent for a relativistically drifting, uniform, cold plasma. In the evanescent regime $\omega < \omega_p\sqrt{2}$, the wave penetrates a few plasma skin depths c/ω_p.

When a TEM wave with $E \gg 1$ is launched into a nonstreaming plasma, its ponderomotive force excavates a density cavity around the antenna. If the energy density of the wave field, $\epsilon_0 E_0^2$, exceeds $n^\pm mc^2$, the cavity expands at relativistic speeds. To verify (1) for a nonstreaming plasma, one would need to set up the wave field and particle distribution self-consistently at all x before starting the simulation (which we defer to a future paper), and even then, one would expect the wave to be disrupted by parametric instabilities (Max & Perkins 1972; Sweeney & Stewart 1975; Ashour-Abdalla et al. 1981; Leboeuf et al. 1982). However, if a nonlinear TEM wave is launched into a streaming plasma ($\gamma_d \gg 1$), it propagates freely — without excavating the plasma and without being disrupted by parametric instabilites — in the regime $\omega > \omega_p\sqrt{2}/(1 + E^2)^{1/4}$. In the parameter ranges $1 < E < 10^3$ and $1 < \gamma_d < 3.9 \times 10^3$, the value of η we compute agrees with (1) to 5 per cent. We stress, however, that more work is needed to rigorously verify that the simulated fields and particle momentum distributions are compatible with the assumption of an infinite, plane TEM wave given by (1).

3.   SHOCKED TEM WAVE

In certain respects, the above PIC experiment with freely propagating TEM waves overlaps with previous works (Ashour-Abdalla et al. 1981; Leboeuf et al. 1982). The main focus of the current work is a different scenario: A nonlinear TEM wave which encounters an ultra-relativistic shock formed by a confining medium, as in the case of a pulsar wind termination shock. In order to simulate such a shock, we repeat the experiment described in §2 but add a particle-reflecting, wave-transmitting magnetic wall in the region $95 \lesssim \hat{x} \equiv x\omega_{p\dagger}/c \lesssim 100$, where $\omega_{p\dagger} = \omega_p(x = 0)$. We trace $O(10^6 - 10^7)$ particles for $O(10^3 - 10^4)$ timesteps on a grid where each cell has a size $\Delta x = \Delta y \lesssim 0.1c\pi/\omega_{p\dagger}$, and the timestep is given by $\Delta t = 0.4\Delta x/c$. The grid has 128 cells and periodic open boundaries in the y-direction, and from 256 to 1600 cells in the x-direction. Below, the antenna (TEM wave) frequency is denoted by ω_0. We observe that the after reflected off the magnetic wall, the counterstreaming particles trigger a Weibel instability, which causes the beam to filament in the y direction. The initial stage of the instability is marked by exponentially growing oscillations (along the y axis) of the magnetic field component B_z, with characteristic wavelength c/ω_p. A shock forms after a time t given by $\omega_{p\dagger}(t - t_{\text{ref}}) \simeq 40 - 70$, where t_{ref} is the instant when the front of the beam reflects off the magnetic wall. As there is no dc magnetic field in our simulations, the cyclotron instability seen by others (Gallant et al. 1992; Hoshino et al. 1992; Spitkovsky &

Arons 2004) is absent.

In the discussion below, we average all quantities over y, smoothing out the filaments. We fix the bulk Lorentz factor at $\hat{x} = 0$ to be $\gamma_0 = 3870$. The value of σ at the antenna, $\sigma(\hat{x} = 0)$, is denoted by Σ_0, and we adopt parameters such that $E(\hat{x} = 0) = 5.4 \times 10^3 (\omega_{p\dagger}/\omega_0)\sqrt{\Sigma_0}$. Downstream from the antenna, the field couples to the particles and quickly reduces E until, at $\hat{x} \approx 25$, a 'fully developed' TEM wave forms, in which $E(\hat{x}) \simeq u_\perp(\hat{x})/c$, where $u_\perp(\hat{x})$ is the local ensemble average of $(u_y{}^2 + u_z{}^2)^{1/2}$ (u_y and u_z are components of the 4-velocity). We refer to the regions $10 \lesssim \hat{x} \lesssim 50$, $50 \lesssim \hat{x} \lesssim 80$, and $\hat{x} \gtrsim 80$ as the shock precursor, the shock interior and the downstream medium, respectively.

3.1. Plasma Heating

In the shock precursor, there is a strong, coherent, position-dependent interaction between the wave and the particles. The lower panels of Fig. 1 show the e^+ number density in $(\hat{x}, u_z)$-space at two different positions. At low $\hat{x}$, the particle motion is almost phase-coherent, but electrostatic and electromagnetic fluctuations gradually increase the thermal spread with $\hat{x}$ until it exceeds the wave-induced quiver motion. The conversion of Poynting flux and kinetic-energy flux into thermal motions is evident from the upper panels of Fig. 1, which show the frequency spectrum of the electric field component E_y. As $\hat{x}$ increases, the thermal background (broad sidebands) grows at the expense of the antenna-driven TEM mode (narrow lines at $\omega = \pm\omega_0$).

The positron energy distribution $f(\gamma)$ is shown at two positions in Fig. 2, one in the shock precursor and the other in the shock interior. Interestingly, for a wave with $\Sigma_0 \gtrsim 1$, we find $\langle\gamma\rangle \propto \gamma_0(\Sigma_0 + 1)$ at both positions (indeed, throughout the shock), although the form of $f(\gamma)$ changes. In the precursor ($8 \lesssim \hat{x} \lesssim 16$), the distribution is narrow and drops quickly at high energies; fitting the tail with a power law, $f(\gamma) \simeq \gamma^{-\alpha}$, we obtain $15 \lesssim \alpha \lesssim 35$ for the range $2 \lesssim \Sigma_0 \lesssim 24$. This does not necessarily imply nonthermal acceleration, but rather the heating of an initially cold distribution. In the shock interior ($50 \lesssim \hat{x} \lesssim 58$), $f(\gamma)$ turns into an anisotropic Maxwellian (see §3.3). The stronger the TEM wave, the hotter the downstream plasma, with $\langle\gamma\rangle$ determined by the *total* upstream energy flux.

The anisotropy of the particle distribution in the shock interior depends on the polarization of the wave; for example, a linearly polarized wave with $E_z \gg 1$ and $E_y = 0$ predominantly energizes u_z. A detailed study of this issue is outside the scope of this paper, which focuses on circularly polarized TEM waves.

3.2. Fate of the Wave

As the wave propagates away from the antenna and accelerates the particles into oscillations, σ quickly drops below Σ_0. For $\hat{x} \gtrsim 25$, E changes little until it encounters the shock, beyond which the wave continues to decay. The decay rate scales with the skin depth, $c/\omega_{p\dagger}$. Figure 3a shows the TEM wave amplitude as a function of position and Σ_0. For $\Sigma_0 = 0.4$, we find $E(\hat{x} = 28)/E(\hat{x} = 0) = 0.05$ and $E(\hat{x} = 40)/E(\hat{x} = 0) \lesssim 0.01$. For $\Sigma_0 = 3.6\,(14.0)$, the corresponding ratios are $0.20\,(0.25)$ and $0.07\,(0.14)$, respectively. In the case $\Sigma_0 = 14.0$, E remains roughly flat for $40 < \hat{x} < 70$, before dropping away for $\hat{x} \gtrsim 70$. The drop is accompanied by a temperature decline, possibly because the plasma near the magnetic wall is not yet thermalized. For $\Sigma_0 \simeq 6$, a similar drops occurs at $\hat{x} \gtrsim 57$.

Taken together with similar simulations spanning the parameter range $1 \lesssim \omega_0/\omega_{p\dagger} \lesssim 10$, Fig. 3a leads to an important result: the length scale L_d over which E drops by two orders of magnitude, scales proportionally to the skin depth as

$$L_d \quad \simeq \quad Kc/\omega_{p\dagger}, \tag{2}$$

where $10^2 \lesssim K \lesssim 10^3$ depends on $\omega_0/\omega_{p\dagger}$; i.e., near (far from) from the cutoff given by (1) the decay is faster (slower). This is consistent with previous results for an unshocked, relativistic EM wave (Leboeuf et al. 1982). The value of K also increases slowly with the amplitude (for $0.2 < \Sigma_0 < 20$ we obtain $50 \lesssim K \lesssim 150$ with $\omega_0/\omega_{p\dagger} \simeq 2.0$). For the parameter regime $\omega_0/\omega_{p\dagger} \gg 10$, which we cannot achieve in our simulations (since it would require a very large number of timesteps to both allow the shock to form and resolve the wave oscillations), the value of K might exceed 10^3. Over distances much greater than L_d, the wave may enter the linear regime, but we are unable to distinguish the wave from the noise at this level in our simulations. (Note that if L_d is redefined as the length scale over which E drops by a factor of e, K is reduced by a factor of 4.6).

As seen from Fig. 3b, as the wave decays the tranverse momentum density $e_\perp(\hat{x}) = n(\hat{x})u_\perp(\hat{x})/c$, where $n(\hat{x}) = n^+(\hat{x}) + n^-(\hat{x})$, increases with $\hat{x}$. The largest-amplitude case ($\Sigma_0 = 14.0$) is an exception, with $\partial e_\perp/\partial \hat{x} < 0$ near $\hat{x} = 0$ and the magnetic wall; this may be due to ponderomotive forces (§3.3), imperfect absorption of the wave by the simulation boundaries, or other boundary effects.

The wave decay might be caused by a parametric instability which sets in when the bulk speed of the flow is reduced in the shock interior. Further simulations are needed to obtain enough statistics to rigorously settle the microphysical aspects of the decay; this is deferred to a forthcoming work.

3.3.   Density Profile

Our code tracks all three vector components of the electromagnetic fields, but only supports electrostatic (Langmuir) fluctuations in two directions. Particles therefore diffuse slower in u_z than in u_x and u_y. In this respect, our simulations are essentially two-dimensional, with an effective adiabatic index $\Gamma \simeq 3/2$ (not $4/3$, as in isotropic 3D). This explains the form of the density profile $n(x)$ in Fig. 4, plotted at $t = t_{\rm ref} + 85\omega_{p\dagger}^{-1}$ for three different wave amplitudes. In the near-hydrodynamic case $\Sigma_0 \simeq 0$ (not shown), the density jump is $n_2/n_1 \simeq 2.8$, where n_1 (n_2) denotes the upstream (downstream) density, consistent with the Rankine-Hugoniot prediction $n_2/n_1 = \Gamma/(\Gamma - 1) \simeq 3$ for $\Gamma = 1.5$. Conversely, given the observed density jump for $\Sigma_0 \simeq 0$, we infer $\Gamma = 1.56$, implying some slow diffusion in u_z. Figure 4 also suggests that n_2/n_1 increases with Σ_0. This trend can be ascribed to the ponderomotive force executed by the decaying TEM wave, and/or by the longitudinal electric field $E_x \propto E$ induced by parametric decay to the Langmuir mode. As the TEM wave decays, we have a ponderomotive force proportional to $\partial E^2/\partial x$; hence n_2/n_1 increases with Σ_0. Interestingly, we see little or no evidence that the shock speed changes with Σ_0.

4.   CRAB PULSAR WIND

For a steady-state pulsar wind, conservation of mass and energy give

$$\frac{\omega_0}{\omega_p} = 4.6 \times 10^{-8} \left(\frac{r}{r_L}\right) \left[\frac{\gamma_d \left(\Omega_w/4\pi\right)}{\dot{N}_{38}}\right]^{1/2}, \tag{3}$$

$$E = 3.1 \times 10^7 \left(\frac{r_L}{r}\right) \left[\frac{\dot{N}_{38}\mu\sigma}{\eta \left(1 + \sigma\right) \left(\Omega_w/4\pi\right)}\right]^{1/2}. \tag{4}$$

In (3) and (4), ω_0 is given by the pulsar spin rate, the total particle injection rate is $\dot{N} = 10^{38}s^{-1}\dot{N}_{38}$, the solid angle filled by the wind is Ω_w, and we define $\mu = L/\dot{N}mc^2$, where L is the pulsar spin-down luminosity. For canonical Crab parameters ($5 \times 10^4 \lesssim \mu \lesssim 5 \times 10^6$; $\eta \simeq 1$, $\Omega_w/4\pi \simeq 0.1 - 1$, $\sigma(r_s) \simeq 3 \times 10^{-3}$, and $r_s/r_L \simeq 2.7 \times 10^9$) (Trümper & Becker 1998; Weisskopf et al. 2000; Kirk & Skjæraasen 2003; Spitkovsky & Arons 2004), we take $\omega_{p\dagger} = \omega_p(r_s)$ and find $1 \lesssim E \lesssim 10$, $9 \times 10^2 \lesssim \omega_0/\omega_{p\dagger} \lesssim 3 \times 10^5$, and $9 \times 10^4 \lesssim L_d/r_L \lesssim 3 \times 10^8$ at the termination shock (using $10^2 \lesssim K \lesssim 10^3$).

In a self-consistent model of the TEM wave, σ can be expressed in terms of the other quantities in (1), (3), and (4) according to Eq. (97) of Melatos & Melrose (1996), viz.

$$\sigma = \frac{\eta}{\beta_d} \left[\frac{1}{\gamma_d^2 \left(1 - \eta^2\right)} - \frac{\omega^4 \left(1 - \eta^2\right)}{4\gamma_d^2\omega_p^4}\right]. \tag{5}$$

This allows us to solve self-consistently for η, σ, E, and $\omega_{p\dagger}$ given just $\dot{N}$ and γ_d. Adopting the current best estimates of these quantities, $\dot{N}_{38} = 10^{0.3}$ and $\gamma_d = 10^6$, as inferred from an ion-cyclotron model of the variability of the Crab wisps (Spitkovsky & Arons 2004), together with $\Omega_w \simeq 4\pi$, we solve (1) and (3)–(5) to obtain $\sigma \simeq 9.0 \times 10^{-3}$, $E \simeq 2.5$, $L_d/r_L \simeq 10^7 - 10^8$, and $1 - \eta \simeq 4.8 \times 10^{-11}$ (the value for η reflects the fact that the displacement current dominates the conduction current for $r > r_c$).

Evidently, our simulations explore artificially small values of $\omega_0/\omega_{p\dagger}$ (for best-guess values, $\omega_0/\omega_{p\dagger} \approx 9 \times 10^4$ at the Crab shock), and artificially large values of σ and E (e.g., in Fig. 4, $\Sigma_0 = 3.6$ gives $\sigma \simeq 0.01$ and $E \simeq 4 \times 10^2$ at $\hat{x} \simeq 50$) due to numerical limitations. Nevertheless, we consistently find $L_d \gtrsim 10^2 c/\omega_{p\dagger}$ for $0.1 \lesssim \Sigma_0 \lesssim 100$, i.e., over three decades in Σ_0. The fate of the TEM wave thus seems clear: It decays beyond r_s, just like the entropy wave (Lyubarsky 2003), but the dissipation mechanism is not reconnection. The decay scale exceeds $10^7 r_L$.

Observationally, L_d might be resolved. It subtends $0.05'' - 0.5''$ if the Crab is at distance of 2 kpc, using $10^2 < K < 10^3$ and the best estimates for the wind parameters. This range includes the angular thickness of filamentary, variable substructure in the equatorial wisps of the Crab pulsar wind, observed by the *Hubble Space Telescope* and the *Chandra X-ray Observatory* (Hester et al. 2002), but at present the connection is speculative. Since L_d increases with $\omega/\omega_{p\dagger}$ in the parameter regime near cutoff, and the Crab shock value of $\omega/\omega_{p\dagger}$ cannot be achieved in our simulations, we can only conclusively give a *lower limit* $(100c/\omega_{p\dagger})$ for L_d; i.e., the possibility that $L_d > 10^3 c/\omega_{p\dagger}$ ($> 0.5''$) cannot be excluded. A theoretical upper limit for L_d can be estimated by noting that, ultimately, adiabatic cooling of the diverging, subrelativistic flow beyond the Crab termination shock enforces a cutoff, and parametric instabilities are bound to set in, yielding $L_d \lesssim O(r_s)$.

The TEM wave generates a latitude-dependent, nonthermal particle distribution inside the shock which is anisotropic near the equatorial plane, where the wave is (approximately) linearly polarized, and isotropic at high latitudes, where the polarization is (approximately) circular. In principle, future X-ray and/or optical polarization measurements can test this prediction.

The simulations reported here do not include a dc magnetic field, as exists for an oblique rotator. Such a field affects the propagation and stability of the TEM wave (Asseo et al. 1980). For example, a subluminal, circularly polarized TEM wave with a dc magnetic field in the x-direction (radially) is stable in the inner part of the wind but unstable to three-wave parametric decay in the outer wind (Melatos 1998, 2002). These important issues will be addressed in a forthcoming paper.

REFERENCES

Akhiezer, A. I., & Polovin, R. V. 1956, Sov. Phys. JETP, 3, 696

Arons, J. 1979, Space Science Reviews, 24, 437

Arons, J. 2002, in Astronomical Society of the Pacific Conference Series, Vol. 271, 71

Ashour-Abdalla, M., Leboeuf, J. N., Tajima, T., Dawson, J. M., & Kennel, C. F. 1981, Phys. Rev. A, 23, 1906

Asseo, E., Llobet, X., & Schmidt, G. 1980, Phys. Rev. A, 22, 1293

Bogovalov, S. V. 1999, A&A, 349, 1017

Chatterjee, S., & Cordes, J. M. 2004, ApJ, 600, L51

Coroniti, F. V. 1990, ApJ, 349, 538

Gaensler, B. M., Arons, J., Kaspi, V. M., Pivovaroff, M. J., Kawai, N., & Tamura, K. 2002, ApJ, 569, 878

Gaensler, B. M., van der Swaluw, E., Camilo, F., Kaspi, V. M., Baganoff, F. K., Yusef-Zadeh, F., & Manchester, R. N. 2004, ApJ, 616, 383

Gallant, Y. A., Hoshino, M., Langdon, A. B., Arons, J., & Max, C. E. 1992, ApJ, 391, 73

Gedalin, M., Gruman, E., & Melrose, D. B. 2001, MNRAS, 325, 715

Hester, J. J., Mori, K., Burrows, D., Gallagher, J. S., Graham, J. R., Halverson, M., Kader, A., Michel, F. C., & Scowen, P. 2002, ApJ, 577, L49

Hoshino, M., Arons, J., Gallant, Y. A., & Langdon, A. B. 1992, ApJ, 390, 454

Kaw, P., & Dawson, J. 1970, Phys. Fluids, 13, 472

Kennel, C. F., & Coroniti, F. V. 1984a, ApJ, 283, 694

—. 1984b, ApJ, 283, 710

Kennel, C. F., & Pellat, R. 1976, J. Plasma Phys., 15, 335

Kirk, J. G. 2004, Physical Review Letters, 92, 181101

Kirk, J. G., & Skjæraasen, O. 2003, ApJ, 591, 366

Kirk, J. G., Skjæraasen, O., & Gallant, Y. A. 2002, A&A, 388, L29

Komissarov, S. S., & Lyubarsky, Y. E. 2004, MNRAS, 349, 779

Kuijpers, J. 2001, Publications of the Astronomical Society of Australia, 18, 407

Leboeuf, J. N., Ashour-Abdalla, M., Tajima, T., Kennel, C. F., Coroniti, F. V., & Dawson, J. M. 1982, Phys. Rev. A, 25, 1023

Lyubarsky, Y., & Kirk, J. G. 2001, ApJ, 547, 437

Lyubarsky, Y. E. 2003, MNRAS, 345, 153

Max, C., & Perkins, F. 1972, Physical Review Letters, 29, 1731

Melatos, A. 1998, Memorie della Societa Astronomica Italiana, 69, 1009

Melatos, A. 2002, in Astronomical Society of the Pacific Conference Series, Vol. 271, 115

Melatos, A., & Melrose, D. B. 1996, MNRAS, 279, 1168

Pétri, J., & Kirk, J. G. 2005, ApJ, 627, L37

Skjæraasen, O. 2004, Advances in Space Research, 33, 586

Spitkovsky, A., & Arons, J. 2004, ApJ, 603, 669

Sweeney, G. S. S., & Stewart, P. 1975, A&A, 41, 431

Trümper, J., & Becker, W. 1998, Advances in Space Research, 21, 203

Verboncoeur, J. P., Langdon, A. B., & Gadd, N. T. 1995, Comp. Phys. Comm., 87, 199

Weisskopf, M. C., Hester, J. J., Tennant, A. F., Elsner, R. F., Schulz, N. S., Marshall, H. L., Karovska, M., Nichols, J. S., Swartz, D. A., Kolodziejczak, J. J., & O'Dell, S. L. 2000, ApJ, 536, L81
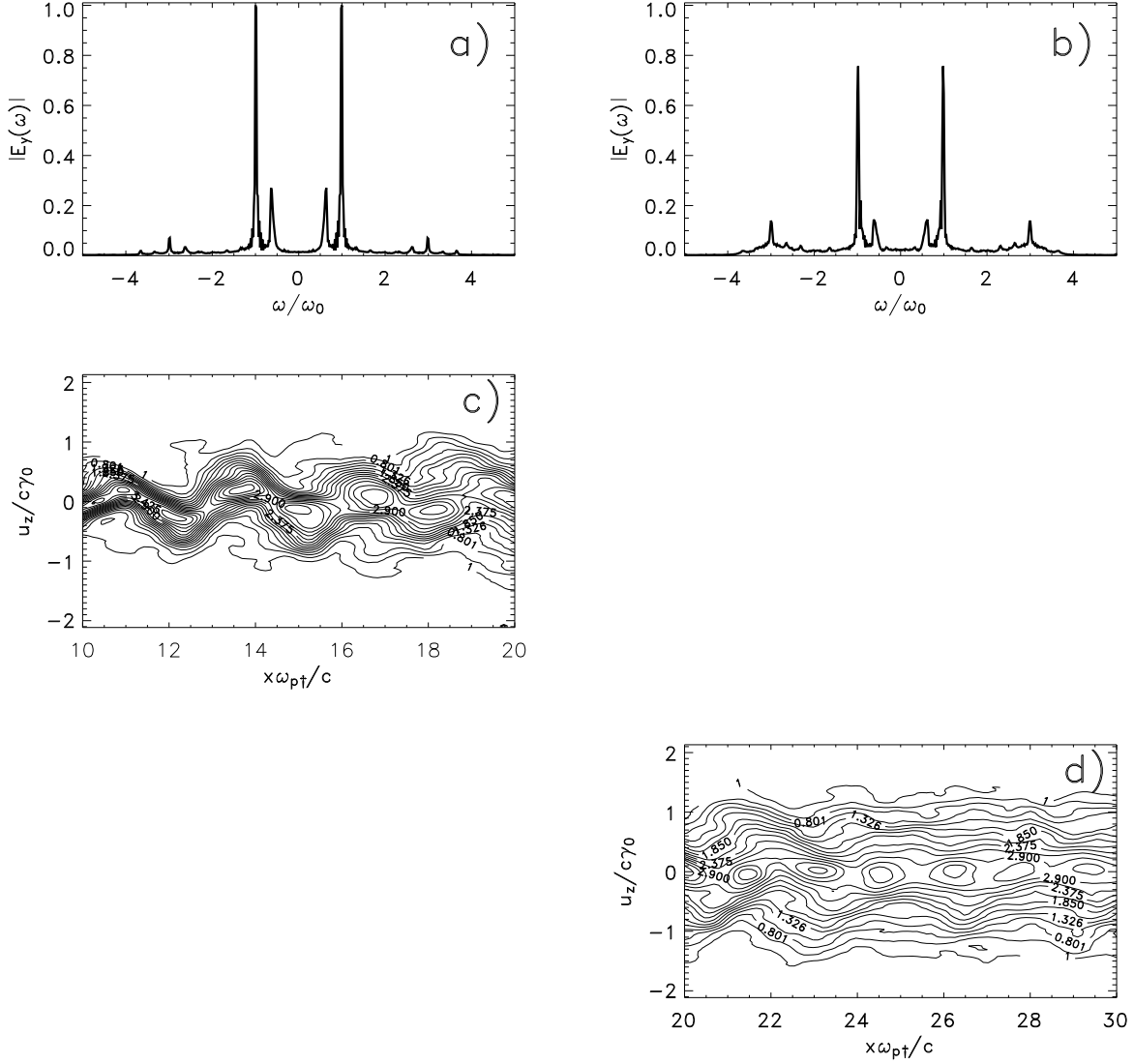
Fig. 1.— The shock precursor. *Top row*: Frequency spectrum $|E_y(\omega)|$ at (*a*) $\hat{x} = 14$ and (*b*) $\hat{x} = 29$, obtained during the time interval $56 \lesssim \omega_{p\dagger}(t - t_{\mathrm{ref}}) \lesssim 80$. The lines at $\omega = \pm\omega_0$ are the nonlinear TEM wave. As $\hat{x}$ increases, the lines decay and broaden while the thermal background spectrum grows. The lines at $\omega \simeq \pm 0.6\omega_0$ are due to electrostatic plasma oscillations. *Bottom row*: Positron density in (x, u_z)-space for (*c*) $10 < \hat{x} < 20$ and (*d*) $20 < \hat{x} < 30$. In (c), the particles are strongly phase-coherent with the wave (which has a wavelength of $\approx 3.3\hat{x}$), although thermal broadening can be seen at $\hat{x} > 11$. In (d), the thermal width is larger than the quiver amplitude, but a periodic modulation is still evident (in the absence of the wave, one gets a straight beam centered on $u_z = 0$, gradually broadening with $\hat{x}$). The parameters used are $\Sigma_0 = 2.0$, $\gamma_0 = 3870$, $\omega_0/\omega_{p\dagger} = 1.97$, $t = t_{\mathrm{ref}} + 85/\omega_{p\dagger}$, and $E(\hat{x} = 0) = 2.0 \times 10^3\sqrt{\Sigma_0}$.
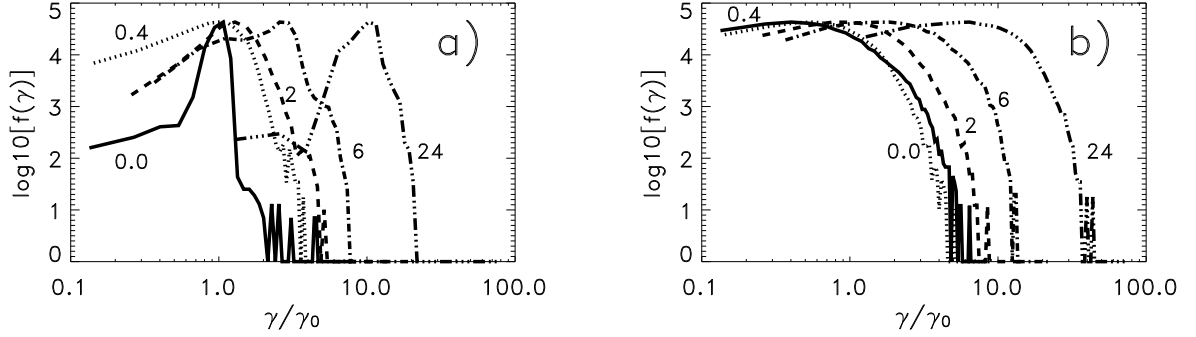
Fig. 2.— The energy distribution $f(\gamma)$ of positrons for $8 < \hat{x} < 16$ (a) and $50 < \hat{x} < 58$ (b), normalized such that $\int d\gamma f(\gamma) = n^+$. The labels denote Σ_0; the other parameters are as in Fig. 1.
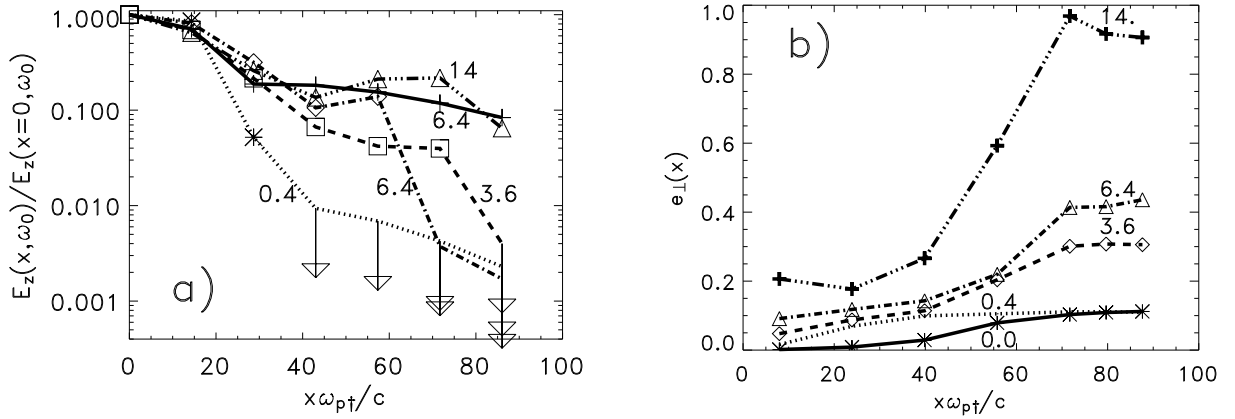

Fig. 3.— (a) Fourier amplitude of the TEM wave at $\omega = \omega_0$ as a function of $\hat{x}$, normalized to its value at $\hat{x} = 0$. The solid line represents free propagation (no shock). The other curves are for shocked TEM waves. Arrows indicate upper limits, and labels denote Σ_0. (b) Transverse momentum density $e_\perp(\hat{x}) = n(\hat{x})u_\perp(\hat{x})/c$, in arbitrary units. As the wave decays, $e_\perp$ increases due to plasma heating. Each curve represents a shocked TEM wave. Both panels are snapshots at $t \simeq t_{\rm ref} + 100\omega_{p\dagger}^{-1}$. Other parameters are as in Fig. 1.
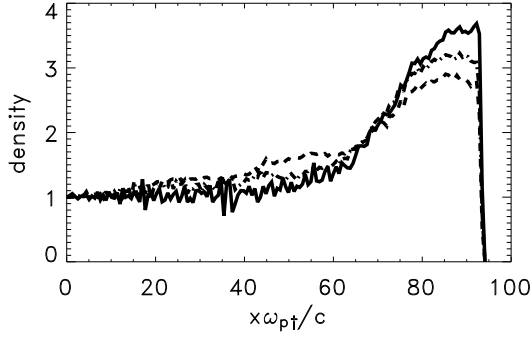
Fig. 4.— The aggregate density profile $n(\hat{x}) = n^+(\hat{x}) + n^-(\hat{x})$ for a TEM wave shock. The regions $10 \lesssim \hat{x} \lesssim 50$, $50 \lesssim \hat{x} \lesssim 80$, and $\hat{x} \gtrsim 80$ are the shock precursor, the shock interior and the downstream medium, respectively (see §2). The drop at $\hat{x} \gtrsim 95$ is due to the magnetic wall. The solid, dashed-dotted, and dashed lines are for $\Sigma_0 = 24$, $\Sigma_0 = 2.0$, and $\Sigma_0 = 0.4$, respectively. Other parameters are as in Fig. 1.